

Precipitation of β -Al₅FeSi Phase Platelets in Al-Si Based Casting Alloys

L. LIU, A.M.A. MOHAMED, A.M. SAMUEL, F.H. SAMUEL, H.W. DOTY,
and S. VALTIERRA

The aim of the present work has been to investigate the factors affecting the precipitation of the β -Al₅FeSi iron intermetallic phase of directionally solidified A356- and 319-type alloys as a function of the iron content, a Sr addition of ~250 ppm, and superheating or cooling rates. The iron levels selected varied from 0.12 to 0.8 wt pct and cover the range of Fe levels in commercial casting alloys. The use of an end-chill mold provided different cooling rates along the height of the same casting, with dendritic arm spacing values that varied from ~15 to 85 μ m, corresponding to levels of 5, 10, 30, 50, and 100 mm above the chill end. The microstructure and phase identification were monitored using optical microscopy, scanning electron microscopy (SEM), thermal analysis, and electron probe microanalysis (EPMA) techniques. An image analyzer was used in conjunction with the optical microscope for quantification purposes. The results showed that, for the range of cooling rates covered in the present study, the highest cooling rate (at a 5-mm distance from the chill) is the more significant parameter in controlling the size and distribution of the β -Al₅FeSi intermetallic phase in the nonmodified 319 and 356 alloys. The addition of strontium leads to fragmentation of coeutectic or posteutectic β platelets. This effect diminishes with an increase in the iron concentration, and further strontium addition leads to the precipitation of Al₂Si₂Sr phase particles, instead.

DOI: 10.1007/s11661-009-9944-8

© The Minerals, Metals & Materials Society and ASM International 2009

I. INTRODUCTION

WITH their characteristics of low specific gravity, low melting point, excellent castability, and good corrosion resistance, aluminum-silicon (Al-Si) alloys are employed extensively for automotive applications. Two of the most popular commercial alloys used in such applications are the 319- and A356-type alloys belonging to the Al-Si-Cu and Al-Si-Mg alloy systems. The casting quality and properties are determined by the quality of their microstructures, which in turn are regulated by various parameters such as the dendrite arm spacing (DAS) (as governed by the solidification rate), the degree of eutectic Si modification and grain refinement, and the amount of microporosity, intermetallics, and inclusions to be observed in the microstructure. Among these, the intermetallics and the solidification rate are the most important, as they directly or indirectly affect almost all the other microstructural parameters.

Iron is the most pervasive impurity to be found in aluminum; it stems from impurities in bauxite ore and

contamination with ferrous metals and oxides during handling and recycling.^[1] This element is known for contaminating Al-Si casting alloys and for being most deleterious with respect to the strength and toughness of the alloy, because it forms the needlelike β -Al₅FeSi intermetallic phase during solidification.^[2-6] Dissolution is the only practical method for reducing the presence of iron in aluminum. The solubility of iron in molten aluminum is high, leading to the eventual dissolution of ferrous material once it comes into contact with molten aluminum. By contrast, iron solubility in solid aluminum is very low, only 0.05 pct at 660 °C.^[7] It is even less at room temperature or in the presence of alloying elements that form compounds with iron. Fine Fe-rich particles precipitate at intermediate temperatures and cannot be dissolved when in the solid state.

Aluminum forms a variety of intermetallic compounds with its alloying elements. Intermetallic compounds are, in fact, solid solutions that have a substantial capacity for dissolving other elements. The composition of these compounds tends to vary, although they are expressed as chemical formulae. During solidification, iron, together with other alloying elements such as Cu, Mg, Zn, Mn, Ti, *etc.*, partly goes into solid solution in the matrix and partly forms intermetallics, including β -Al₅FeSi and α -Al₁₅Fe₃Si₂ phases.^[8] The Chinese script morphology of the α -Fe phase occurs during eutectic solidification, while the α -Fe phase may also appear in the form of polyhedrons if it solidifies as a primary phase.^[9,10] The β -Fe phase is largely associated with iron levels greater than ~1 pct Fe, found roughly at the location of the eutectic trough

L. LIU and A.M. SAMUEL, Doctors, and F.H. SAMUEL, Professor, are with Applied Science, Université du Québec a Chicoutimi, Chicoutimi, QC, Canada G7H 2B1. Contact e-mail: fhsamuel@uqac.ca A.M.A. MOHAMED, Doctor, Metallurgical and Materials Engineering, Université du Québec a Chicoutimi, is on the Faculty of Petroleum and Mining Engineering, Suez Canal University, Box 43721, Suez, Egypt. H.W. DOTY, Doctor, is with the General Motors Powertrain Group, Metal Casting Technology, Inc., Milford, NH 03055. S. VALTIERRA, Doctor, is with Corporativo Nemark, Garza Garcia, NL, 66221, Mexico.

Manuscript submitted June 4, 2007.

Article published online August 19, 2009

on the Al-Si-Fe phase diagram. Sufficient iron segregation occurs during solidification, however, to cause the β phase to form, even when the iron level is much less than 1 pct.^[11]

The β -Al₅FeSi phase is considered to be the most critical of the iron intermetallics, because it significantly reduces alloy ductility and fracture toughness. This phase manifests/exists in the form of thin platelets that appear as needles in the microstructure; the size of these platelets or needles is controlled by the iron content and the solidification conditions of the alloy.^[12,13] By contrast, the α -Fe phase is less deleterious to the mechanical properties because of its compact morphology.

The satisfactory regulation of the iron level is thus important from a technical point of view, especially where the production of critical components is concerned. A number of different measures have been adopted with a view to neutralizing the harmful effects of the β -Fe phase. These include the following: (1) rapid solidification,^[14,15] (2) addition of neutralizers such as Mn, Co, and Cr,^[12] (3) melt superheat, (4) strontium modification,^[16,17] and (5) nonequilibrium solution heat treatment.^[18]

In view of the importance of the Fe-rich intermetallic phases in aluminum alloys, the present investigation was undertaken to study the factors affecting the precipitation of the β -Al₅FeSi iron intermetallic phase of directionally solidified A356- and 319-type alloys as a function of the iron content, the Sr addition of ~250 ppm, and the cooling rates. Qualitative and quantitative approaches were taken for this purpose.

II. EXPERIMENTAL

The 319 and 356.2 as-received alloys, in the form of 12.5-kg ingots, were cut into smaller pieces, cleaned, dried, and melted in a 7-kg-capacity SiC crucible using an electrical resistance furnace. The melting temperature was maintained at 750 ± 5 °C. The melts were degassed using pure dry argon injected into the melt by means of a graphite rotary degassing impeller. The degassing time/speed was kept constant at 30 min/150 rpm.

Additions of iron were made to the base alloys using an Al-25 pct Fe master alloy, to obtain Fe levels of 0.12, 0.2, 0.4, 0.6, and 0.8 pct, in order to study the amount of β -Al₅FeSi iron phase formed. Strontium additions of 250 ppm were made using an Al-10 pct Sr master alloy, to compare modified with nonmodified structures. Table I lists the chemical analyses of the various alloys studied and their respective codes, as obtained from samplings for the chemical analysis taken from the corresponding melts. With respect to the alloy codes, the prefix A represents the A319.2 alloy, B the B319.2 alloy (containing 0.4 pct Mg), and C the A356.2 alloy. The letter F represents Fe, while the numbers 1, 2, 4, 6, and 8 correspond to the Fe levels of 0.12, 0.2, 0.4, 0.6, and 0.8 pct, respectively. The suffixes 0, 1, 3, 5, and C denote the levels 5, 10, 30, 50, and 100 mm, respectively, above the chill end (*i.e.*, cooling rates corresponding to DASs of 16, 23, 47, 61, and 83 μ m for the 319 alloys and 15, 23, 39, 53, and 75 μ m for the A356.2 alloys). Finally, the suffix S in any code implies that alloy has been Sr-modified. Also, all rows in Table I corresponding to

Table I. Chemical Composition of Various Alloys Used in the Present Work and Their Respective Codes

Alloy Code	Element (Wt Pct)									
	Si	Fe	Cu	Mn	Mg	Cr	B	Sr	Ti	Al
A319.2	6.06	0.120	2.98	0.02300	0.00200	—	—	0.00030	0.0070	bal
AF2	6.83	0.264	3.46	<0.00050	<0.00500	<0.00055	0.00152	<0.00013	0.0030	bal
AF2S	6.36	0.254	3.56	<0.00050	<0.00611	<0.00050	0.00161	0.05190	0.0033	bal
AF4	6.84	0.466	3.56	<0.00050	<0.00500	0.0007	0.0025	<0.00010	0.0028	bal
AF4S	6.19	0.420	3.43	<0.00050	<0.00500	0.0058	0.00238	0.03450	0.0030	bal
AF6	5.29	0.667	3.56	0.00130	<0.00500	<0.00061	0.00365	<0.00095	0.0027	bal
AF6S	6.09	0.638	3.41	0.00070	<0.00500	0.001	0.00348	0.03420	0.0031	bal
AF8	5.31	0.851	3.680	0.00210	<0.00500	0.0008	0.00449	<0.00010	0.0028	bal
AF8S	6.14	0.847	3.430	0.00150	<0.00500	0.0015	0.00449	0.03440	0.0031	bal
B319.2	6.22	0.150	3.210	0.02600	0.40000	—	—	—	0.0075	bal
B4	6.54	0.451	3.320	0.02550	0.40300	0.001	0.00259	0.00040	0.0098	bal
B4S	6.55	0.046	3.260	0.02500	0.39200	0.001	0.00257	0.02260	0.0096	bal
B8	6.50	0.877	3.620	0.10500	0.40700	0.0011	0.00456	<0.00010	0.1000	bal
B8S	6.59	0.879	3.630	0.10200	0.40100	0.0012	0.00451	0.02150	0.0981	bal
A356.2	6.78	0.110	0.020	0.04000	0.33000	—	—	—	0.0800	bal
CF1	7.29	0.112	0.014	0.03670	0.35200	0.0016	0.00061	<0.00012	0.0766	bal
CF1S	7.11	0.109	0.015	0.03610	0.34800	0.0016	0.00054	0.02660	0.0793	bal
CF2	7.25	0.213	0.052	0.03540	0.33900	0.0015	0.00110	0.00020	0.0776	bal
CF2S	7.40	0.249	0.014	0.03660	0.34400	0.0015	0.00130	0.02500	0.0776	bal
CF4	7.27	0.411	0.015	0.03640	0.33600	0.0017	0.00210	<0.00010	0.0768	bal
CF4S	7.20	0.439	0.014	0.03690	0.35100	0.0017	0.002310	0.03750	0.0757	91.77
CF6	7.19	0.645	0.018	0.03750	0.33300	0.0017	0.00332	<0.00010	0.0755	91.63
CF6S	7.26	0.647	0.017	0.03720	0.347	0.0017	0.00332	0.04010	0.0748	91.50
CF8	7.17	0.877	0.015	0.03750	0.338	0.0018	0.00468	<0.00012	0.0735	91.41
CF8S	7.14	0.821	0.027	0.03760	0.334	0.0019	0.00417	0.03510	0.0753	91.46

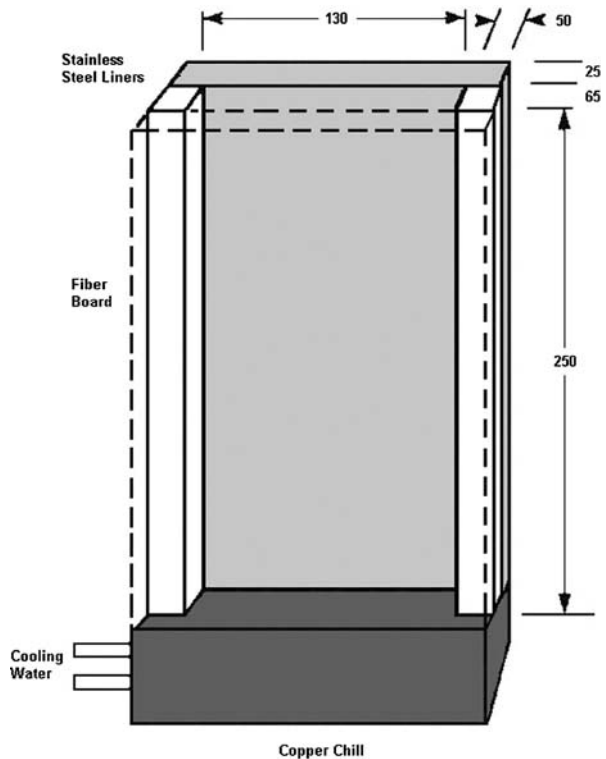


Fig. 1—Schematic diagram of the end-chilled mold used to prepare castings.

Sr-modified alloys have been given a light gray background, to distinguish them from the nonmodified alloys. The chemical analysis was carried out using arc spark spectroscopy at the General Motors facilities (Milford, NH).

A schematic diagram of the rectangular-shaped end-chill mold required for the relevant procedures and measuring $64 \times 127 \times 254$ mm is shown in Figure 1. In order to obtain directional solidification, the four walls of the mold are made of refractory material with a water-chilled copper base.

The molten metal was poured into the mold through ceramic foam filter disks fitted into the riser to avoid incidental inclusions. The mold was preheated to 150°C to dispel any unwanted moisture. The water, which circulates in the copper base, was turned on as soon as the liquid metal had half-filled the mold. Such an arrangement produced ingot blocks with solidification rates that decreased with increasing distance from the chill end, resulting in microstructures that exhibited varying DASs ranging from 15 to $85\ \mu\text{m}$ along the height of the cast block.

In the case of the chill-end castings, specimen blanks were sectioned from the cast blocks at selected heights of 5, 10, 30, 50, and 100 mm above the chill end, corresponding to DAS values ranging between ~ 15 and $\sim 85\ \mu\text{m}$ (Figure 2). Samples 2×3 cm in dimension were cut from the central part of each blank and then mounted in Bakelite and polished to a fine finish ($1\text{-}\mu\text{m}$ diamond paste).

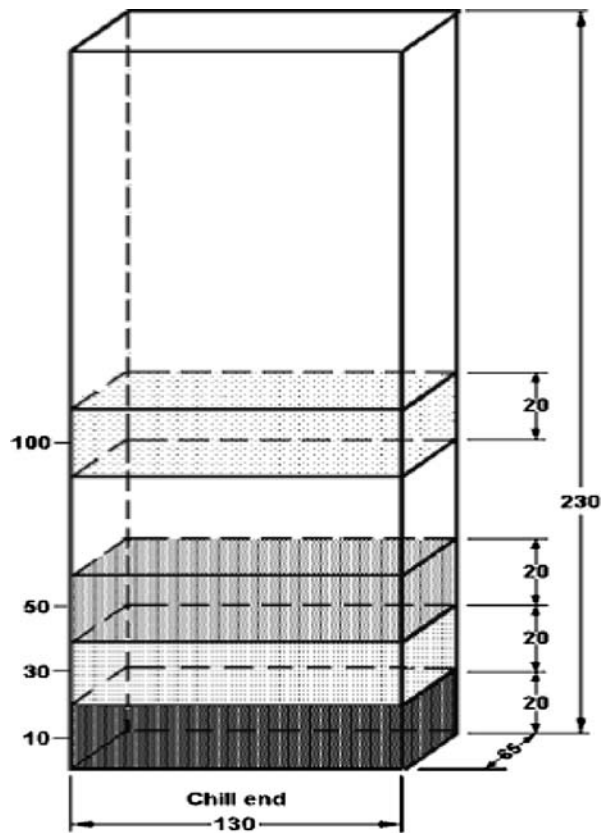


Fig. 2—End-chill casting showing specimen blank sectioning scheme (millimeters).

Quantitative measurements of the $\beta\text{-Al}_5\text{FeSi}$ platelets (or needles, as they appear in the two-dimensional sample surface under the microscope) were made using a

*LECO is a trademark of Leco Corporation, St. Joseph, MI.

LECO* 2001 image analyzer in conjunction with an Olympus BH2-UMA optical microscope (Olympus, Melville, NY). A certain number of fields were examined for each sample, selected in each case so as to cover the entire area of the sample in a regular and systematic fashion. It should be noted that the term “field,” as used here, represents the field of view of the optical microscope and covers an area $2.2608 \times 10^4\ \mu\text{m}^2$ in size at a 500-times magnification.

As regards the $\beta\text{-Al}_5\text{FeSi}$ platelet measurements, the three longest β platelets were measured in each field and, depending upon the sample, 100 to 150 β -platelet measurements were made to obtain the average maximum β -platelet length. By measuring the average thickness of the β -phase platelets, the volume fraction of the β -Fe phase observed in each sample was also determined. In addition, the number of platelets in each field was also counted so as to obtain the β -platelet density. The data were analyzed using statistical software programs by means of which histograms and plots were produced that show the actual β -platelet length distributions and densities obtained.

Phase identification was carried out using scanning electron microscopy (SEM) and electron probe microanalysis (EPMA), in conjunction with energy-dispersive X-ray (EDX) and wavelength dispersion spectroscopic analyses, using a JEOL** JXA-89001 WD/ED com-

**JEOL is a trademark of Japan Electron Optics Ltd., Tokyo.

bined analyzer operating at 20 kV and 30 nA, for which the electron beam size was $\sim 2 \mu\text{m}$.

III. RESULTS AND DISCUSSION

In Al-Si cast alloys, solidification begins with the development of a dendrite network of primary α -Al. The secondary DAS (SDAS, frequently referred to simply as DAS) is essentially determined by the alloy composition, cooling rate, local solidification time, and temperature gradient. It has been shown that the DAS varies with the cooling rate according to the relation^[19]

$$\log(dT/dt) = -[\log(\text{DAS}) - 2.37]/0.4$$

where the cooling rate dT/dt is given in degrees Celsius per minute and the DAS is in micrometers. At any particular location in the casting, the local solidification time determines the DAS and, hence, the mechanical properties. Thus, the DAS is a microstructural manifestation of the cooling rate of a solidifying sample: the higher the cooling rate, the finer the DAS of the sample microstructure, and *vice versa*. In fact, the DAS is often preferred to the cooling rate as an indicator of the solidification conditions of the casting, because it is more accessible to measurement and it incorporates the influence of the other solidification parameters, as well. A finer DAS refines and disperses the porosity and second-phase constituents more evenly (*e.g.*, the β -iron phase). This refinement of the microstructure leads to a substantial improvement in mechanical properties.^[20,21] For example, Figure 3 shows the DAS values obtained from Sr-modified A319.2 and A356.2 alloy samples as a

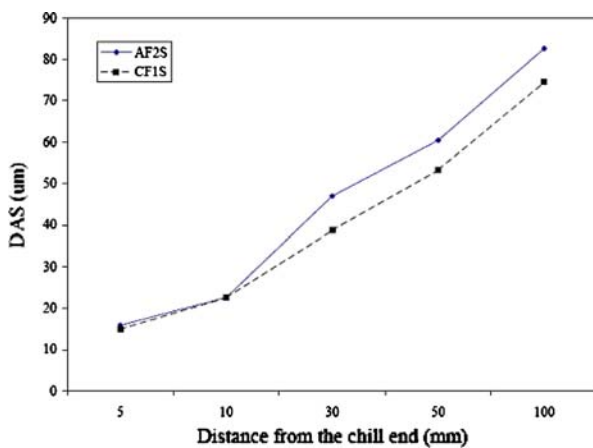


Fig. 3—Dependence of DAS on the cooling rate (AF2S: Sr-modified A319.0.2 pct Fe alloy, CF1S: Sr-modified A356.2 alloy).

function of the distance from the chill end (*i.e.*, the cooling rate).

A. Characterization of Microstructures

Figures 4 through 8 display the microstructures of selected samples that correspond to the three alloy types. The optical micrographs shown in these figures were taken from samples corresponding to the two extreme conditions of the Fe level and cooling rate: low Fe/high cooling rate, and high Fe/low cooling rate, in order to emphasize or compare the microstructural differences between “optimum” and “poor” alloy conditions. The qualitative analyses of the microstructures were supported by quantitative image-analysis results of measurements recorded for area fractions and the average size of the β -iron intermetallics observed in these samples.

1. Alloy A319.2

A typical microstructure obtained from the A319.2 alloy is shown in Figure 4. The various phases, marked 1 through 6, that tend to precipitate are as follows: (1) an α -Al dendrite, (2) a pre-eutectic β -Al₅FeSi particle (big, thick needle), (3) a eutectic Si particle, (4) a posteutectic β -Al₅FeSi particle (thin needle), (5a) a blocklike Al₂Cu particle, (5b) a eutectic (Al + Al₂Cu) particle, and (6) an Al₅Mg₈Cu₂Si₆ particle.^[22]

In Figure 5(a), very fine β needles are observed in the microstructure, often at the interface of the α -Al dendrites or eutectic Si particles, indicating that they precipitated in a coeutectic or posteutectic reaction. The fine eutectic Si particles in Figure 5(b) show that the alloy is well modified.

Figures 5(c) and (d) show examples of the microstructure exhibited by the nonmodified and Sr-modified AF8-C alloy sample (high Fe/low cooling rate condition), respectively. The optical micrograph of Figure 5(c) shows two distinct types of β -Al₅FeSi platelets (or needles, as they appear in the micrograph): large pre-eutectic β and smaller coeutectic or posteutec-

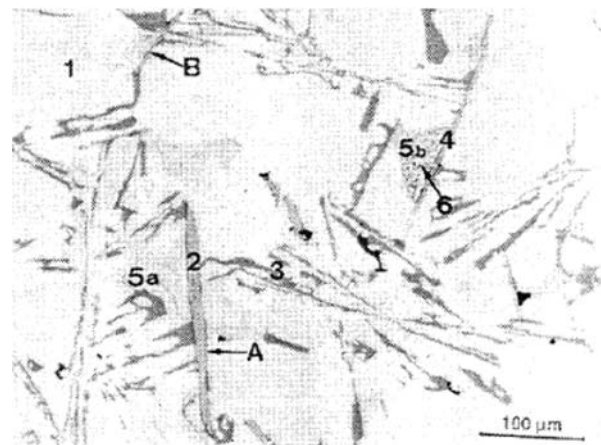


Fig. 4—Optical microstructure of as-solidified A319.2 alloy showing precipitation of: (1) α -Al dendrite, (2) pre-eutectic β -Al₅FeSi, (3) eutectic Si, (4) posteutectic β -Al₅FeSi, (5a) blocklike Al₂Cu, (5b) eutectic Al + Al₂Cu, and (6) Al₅Mg₈Cu₂Si₆ phase particles.^[8]

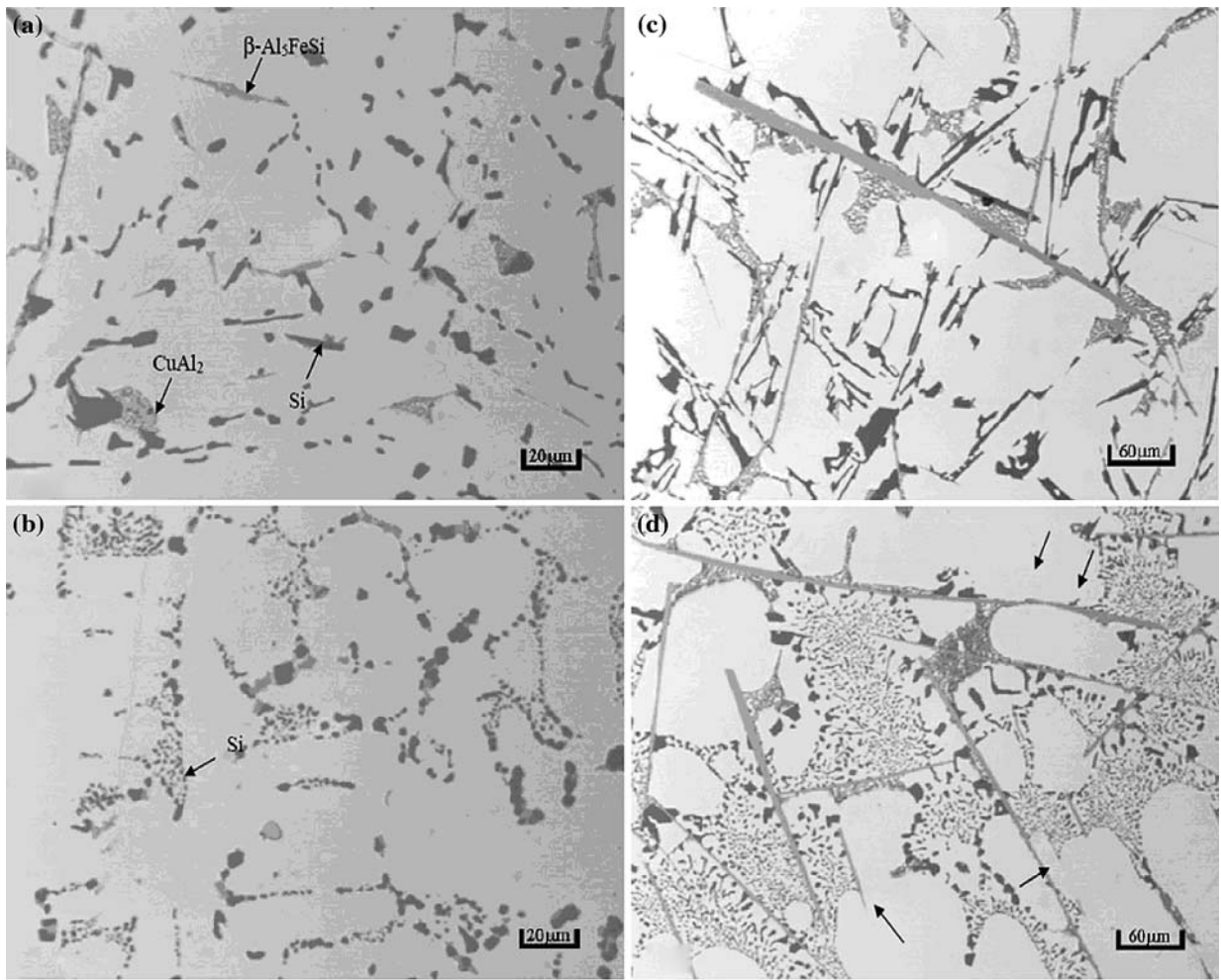


Fig. 5—Optical microstructures of (a) AF2-0, (b) AF2S-0, (c) AF8-C, and (d) AF8S-C alloys. Arrows refer to the effect of Sr on the fragmentation and dissolution of β - Al_5FeSi phase.

tic β , corresponding to their sequence of precipitation with respect to the Al-Si eutectic reaction. The acicular eutectic Si particles indicate the unmodified nature of the alloy.

The backscattered image taken from the same sample, Figure 6, clearly reveals the platelet form of the β - Al_5FeSi phase in which the presence of the pore associated with the platelets assists in revealing the true morphology of the β phase itself. In comparison with the extremely large pre-eutectic β platelet observed at the top of the image, the β platelets within the pore show the much smaller size of what are most likely coeutectic or posteutectic β - Al_5FeSi phase platelets. It is interesting to note the presence of the eutectic Si regions associated with the platelet near the bottom left of the image.

The difference in the size of the β - Al_5FeSi -phase platelet is related to the rate of diffusion of iron atoms with respect to the temperature at which the two platelet types precipitate. Mascré^[23] confirmed that, due to their size and shape, the pre-eutectic β - Al_5FeSi phase platelets are the most pernicious in contributing to the deterioration of alloy mechanical properties. Due to feedability

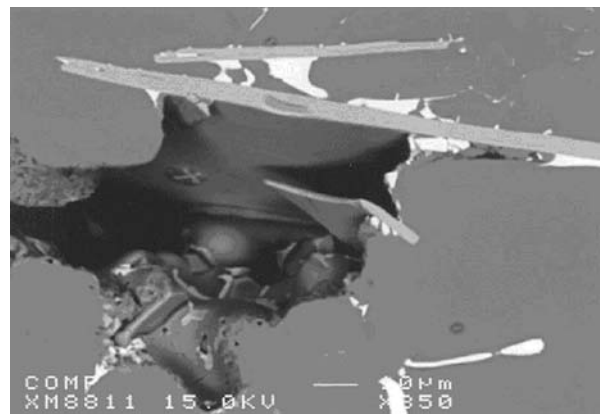


Fig. 6—Backscattered image taken from the AF8-C alloy.

problems related to the plateletlike nature of the β phase, the occurrence of porosity may often be observed in association with the β platelets.

As regards the modified alloy obtained under the same conditions (AF8S-C alloy, Figure 5(d)), while the

eutectic Si regions were well modified by the addition of Sr, its effect on the fragmentation and dissolution of β platelets was observed for the smaller-sized (and thinner) β particles (arrows), whereas the large pre-eutectic β remained unaffected. The persistence of such massive β platelets in the microstructure provides a good indication of why the properties of alloys containing Fe levels of 0.8 pct or higher cannot be improved by any means and, hence, why such alloys should be rejected.

2. Alloy B319.2

Typical microstructures of the B319.2 alloys containing 0.4 and 0.8 Fe are shown in Figure 7. Alloy B319.2 is a higher-Mg-containing version of alloy A319.2 used for applications in the automotive industries. The high Mg content (0.4 pct) leads to the precipitation of Mg_2Si or a Mg-rich phase, which appears in the form of rounded black particles dotted along the sides of the eutectic Si particles,^[22] as may be observed clearly in Figure 7(d) and to some extent in Figure 7(c) (open arrows in both figures).

It is interesting to note the difference in appearance of the eutectic Si particles in these figures, where Mg is also known to modify the eutectic Si. As a result of the

presence of 0.026 pct Mn in the alloy, several α -iron intermetallics may also be observed in the microstructure of the B8-C alloy.

3. A356.2 alloy

Figures 8(a) and (d) show examples of the microstructures of the low-Fe alloy samples obtained at the highest cooling rate. All of the microconstituents are fine in nature and, as the high-magnification micrograph of Figure 8(b) shows, the eutectic Si regions are well modified in the CF1S-0 sample, as are the β platelets (arrowed).

The optical micrograph in Figure 8(c) shows the presence of a large number of β - Al_5FeSi platelets under the 0.8 pct Fe level, the lowest cooling rate conditions. The high-magnification micrograph in Figure 8(d) reveals the dimensions of the pre-eutectic β platelets and the partial transformation of the β platelets into the $Al_8Mg_3FeSi_6$ phase in two cases (arrowed), on account of the magnesium present in the alloy.

Figure 8(e) shows a further example of the same alloy in the modified condition, as obtained at a 50-mm level above the chill end, showing the profusion of β platelets in the microstructure. The high-magnification

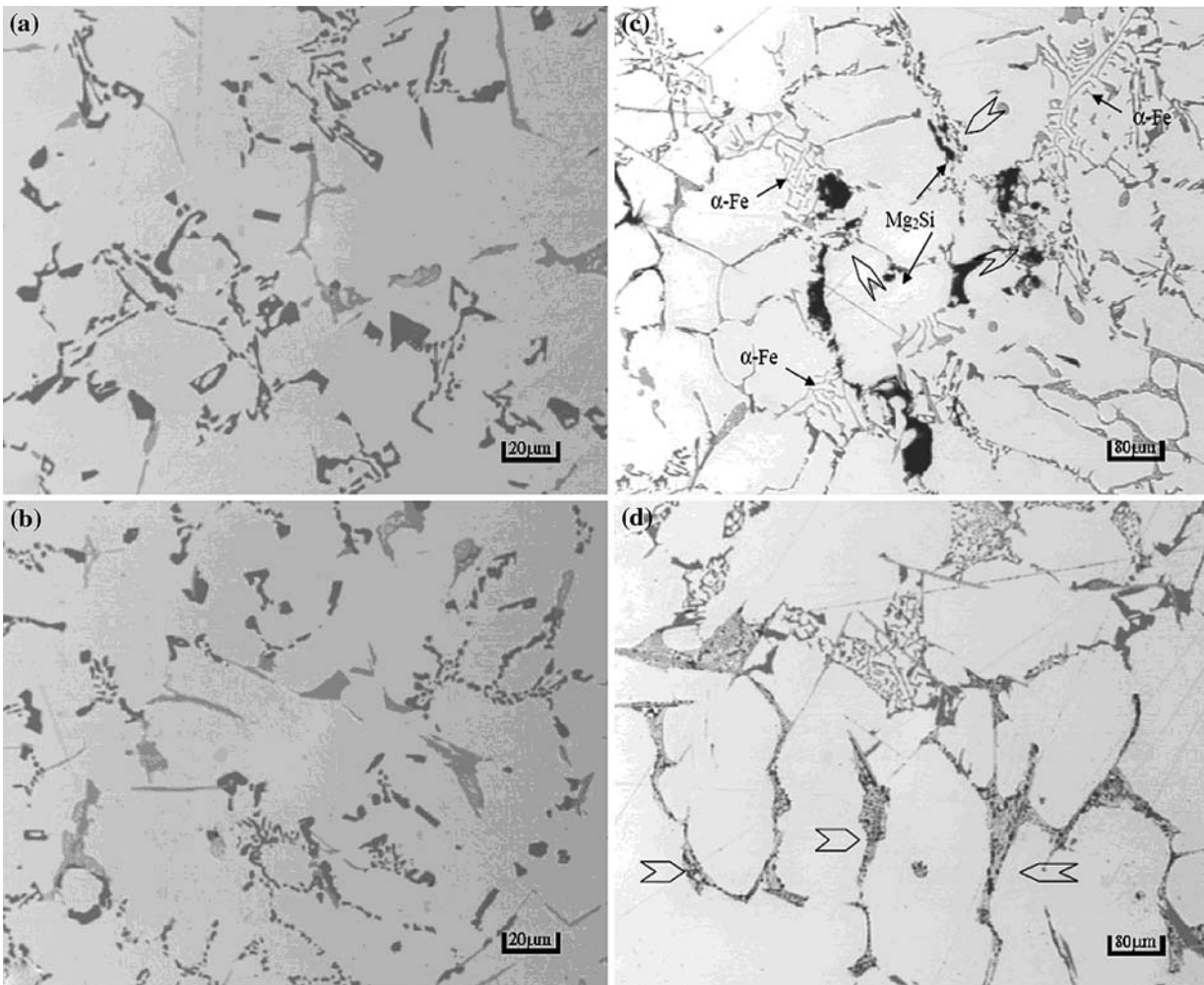


Fig. 7—Optical microstructures of (a) B4-0, (b) B4S-0, (c) B8-C, and (d) B8S-C alloys. Arrows refer to the precipitation of Mg_2Si phase.

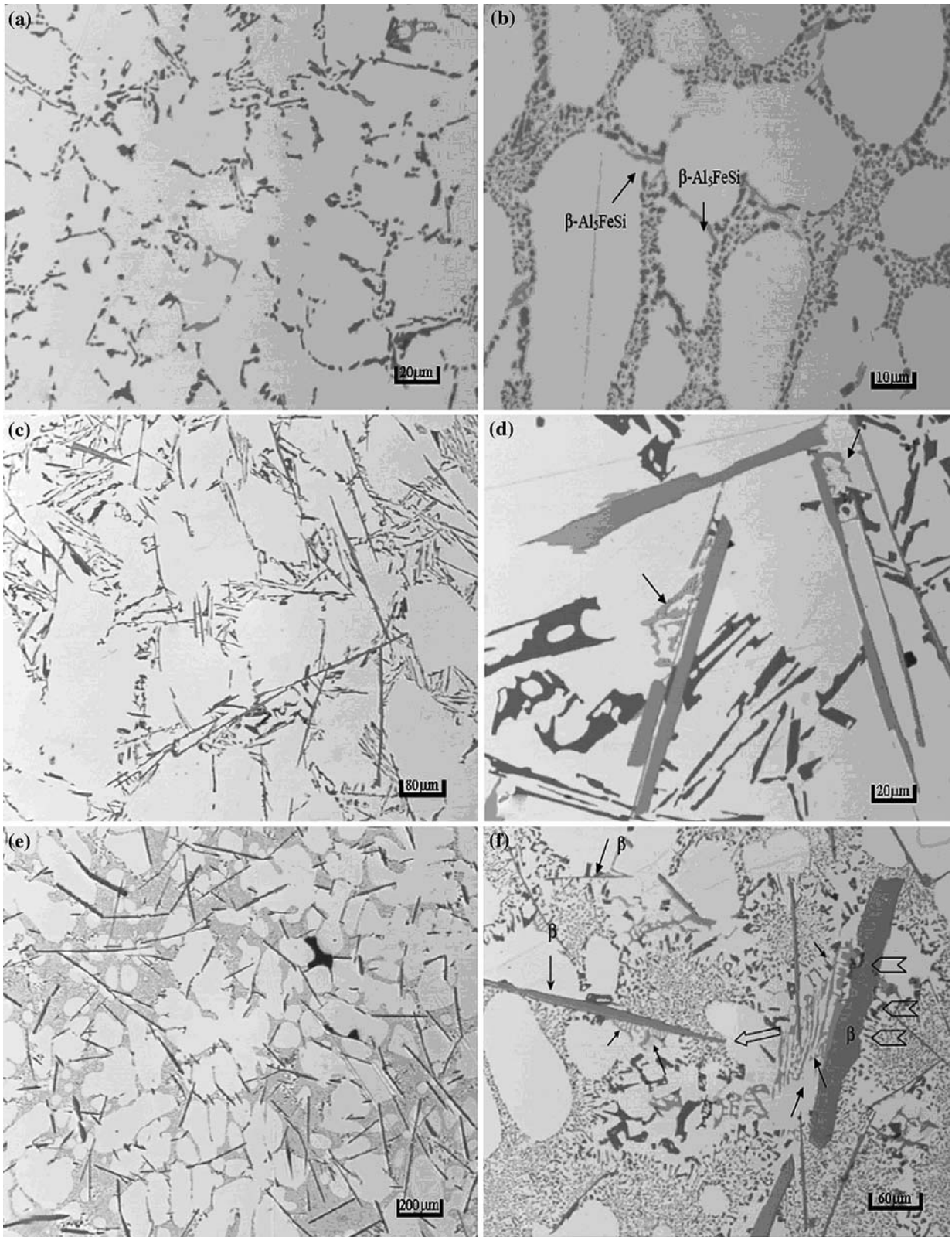


Fig. 8—Optical microstructures of (a) CF1-0, (b) CF1S-0, (c) CF8-C, (d) CF8-C, (e) CF8S-C, (f) CF8S-C alloys. Note that (d) and (c) are at high magnification.

micrograph in Figure 8(f) shows the three types of β platelets that occur, the well-modified eutectic Si regions, and the partial transformation of the large

β platelets (on the right) and long β platelets (on the left) into the $\text{Al}_8\text{Mg}_3\text{FeSi}_6$ phase (small black arrows). Note the irregular contours of the β platelets that are affected

Table II(a). β -Platelet Characteristics Obtained for Nonmodified A319.2 Alloy Samples

Alloy Code	Average Maximum β -Platelet Length (μm)	SD*	Density (No./ mm^2)
AF2-0	31.81	18.16	351.63
AF2-1	47.79	22.25	265.30
AF2-3	64.92	39.86	63.11
AF2-5	89.63	49.23	75.51
AF2-C	117.72	63.84	91.05
AF4-0	31.02	12.59	456.03
AF4-1	33.29	19.45	364.98
AF4-3	99.98	44.69	172.36
AF4-5	146.58	76.47	129.51
AF4-C	143.14	88.17	154.31
AF6-0	32.59	13.9	1612.97
AF6-1	66.68	28.32	656.96
AF6-3	142.34	59.88	130.92
AF6-5	210.55	104.56	66.09
AF6-C	253.76	158.86	49.45
AF8-0	50.66	23.78	2311.53
AF8-1	65.88	34.91	988.19
AF8-3	190.56	95.35	145.68
AF8-5	218.3	118.44	103.92
AF8-C	204.75	146.52	75.04

*SD = standard deviation.

Table II(b). β -Platelet Characteristics Obtained for Sr-Modified A319.2 Alloy Samples

Alloy Code	Average Maximum β -Platelet Length (μm)	SD*	Density (No./ mm^2)
AF2S-0	17.61	11.6	12.56
AF2S-1	36.69	21.19	120.09
AF2S-3	88.2	44.4	92.93
AF2S-5	131.65	74.27	97.48
AF2S-C	136.89	68.46	86.18
AF4S-0	27.58	13.43	387.74
AF4S-1	41.22	24.09	637.34
AF4S-3	101.23	53.54	167.97
AF4S-5	141.1	79.45	190.26
AF4S-C	137.71	81.49	132.33
AF6S-0	61.08	27.4	1116.13
AF6S-1	64.67	26.89	785.68
AF6S-3	184.02	123.61	158.55
AF6S-5	209.85	117.18	104.71
AF6S-C	238.82	167.89	77.71
AF8S-0	56.88	32.74	1099.64
AF8S-1	80.37	33.26	627.92
AF8S-2	187.65	110.3	137.83
AF8S-3	264.96	131.14	131.71
AF8S-C	318.5	255.84	84.14

*SD = standard deviation.

by the Sr or that exist where the transformation takes place (open arrow heads), and the thinning of the long β platelet at its end (open arrow).

B. Platelet Characteristics of β -Al₅FeSi

Tables II through IV list the data for the β -platelet characteristics of average maximum length and density,

Table III. β -Platelet Characteristics Obtained for Nonmodified and Sr-Modified B319.2 Alloy Samples

Alloy Code	Average Maximum β -Platelet Length (μm)	SD	Density (No./ mm^2)
B4-0	31.39	14.15	819.43
B4-1	56.26	28.84	543.93
B4-2	115.12	55.75	157.29
B4-3	160.97	76.79	111.46
B4-C	193.62	113.92	62.32
B8-0	46.89	16.85	1969.31
B8-1	72.31	28.99	1353.95
B8-2	167.52	73.31	331.54
B8-3	235.37	110.35	216.16
B8-C	293.31	179.86	109.89
B4S-0	30.83	12.13	726.82
B4S-1	40.22	18.45	543.15
B4S-2	108.61	67.63	124.96
B4S-3	145.58	61.82	92.62
B4S-C	93.88	36.32	702.33
B8S-0	34.24	11.59	1934.77
B8S-1	56.46	24.04	1350.81
B8S-2	193.82	116.98	312.39
B8S-3	286.14	232.75	204.70
B8S-C	308.62	202.94	133.90

Table IV(a). β -Platelet Characteristics Obtained for Nonmodified A356.2 Alloy Samples

Alloy Code	Average Maximum β -Platelet Length (μm)	SD	Density (No./ mm^2)
CF1-0	10.78	5.72	51.80
CF1-1	14.36	7.1	14.13
CF1-2	34.92	15.38	13.19
CF1-3	30.72	16.41	2.83
CF1-C	45.86	39.25	8.48
CF2-0	12.53	5.49	204.86
CF2-1	12.12	5.89	94.97
CF2-2	29.25	12.87	32.02
CF2-3	38.25	20.32	37.36
CF2-C	45.52	23.91	47.72
CF4-0	17.68	8.94	167.18
CF4-1	29.65	13.28	316.31
CF4-2	77.25	31.41	118.68
CF4-3	119.93	76.3	101.25
CF4-C	130.17	42.36	89.16
CF6-0	27.89	13.41	1105.14
CF6-1	53.9	24.44	612.22
CF6-2	150.95	73.88	183.67
CF6-3	212.41	110.32	112.55
CF6-C	249.96	139.73	79.59
CF8-0	66.65	29.89	795.89
CF8-1	78.05	35.7	352.42
CF8-2	182	107	99.53
CF8-3	274.32	209.36	87.44
CF8-C	236.54	121.27	75.04

SD = standard deviation.

as obtained from the 319 and 356 alloys under non-modified and Sr-modified conditions. Here, the A319.2, B319.2 (containing a higher level of Mg), and A356.2 alloys are represented by the code letters A, B, and C,

Table IV(b). β -Platelet Characteristics Obtained for Sr-Modified A356.2 Alloy Samples

Alloy Code	Average Maximum β -Platelet Length (μm)	SD	Density (No./ mm^2)
CF1S-0	12.79	4.84	848.48
CF1S-1	17.5	8.46	314.74
CF1S-2	23.88	9.64	70.95
CF1S-3	28.27	14.73	87.59
CF1S-C	31.41	18.1	32.65
CF2S-0	8.8	3.33	1041.7
CF2S-1	18.32	9.38	361.05
CF2S-2	26.98	14.68	313.96
CF2S-3	44.48	20.17	100.00
CF2S-C	65.9	37.72	102.19
C4SB-0	24.49	11.11	1295.08
C4SB-1	30.62	11.94	1298.22
C4SB-2	38.02	16.54	1372.00
C4SB-3	62.92	31.29	1903.38
C4SB-C	81.49	49.6	1009.58
C6SB-0	38.47	15.74	1744.44
C6SB-1	43.81	19.71	873.20
C6SB-2	105.91	45.43	280.37
C6SB-3	151.58	95.59	192.77
C6SB-C	197.41	101.43	129.35
CF8S-0	68.81	29.31	842.98
CF8S-1	173.67	93.54	207.84
CF8S-2	199.71	115.57	133.75
CF8S-3	233.84	128.26	120.25
CF8S-C	219.87	120.19	62.48

Note: Codes C4SB and C6SB correspond to castings that were repeated for CF4S and CF6S alloys, respectively.

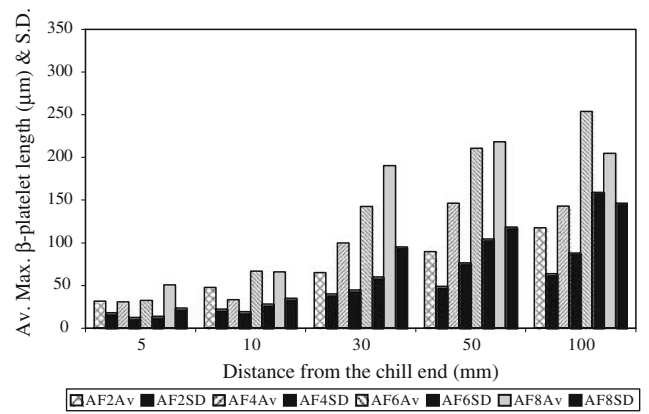
respectively; F1 through F8 represent the iron contents of 0.1, 0.2, 0.4, 0.6, and 0.8 pct; and the suffixes 0, 1, 3, 5, and C (or 0, 1, 2, 3, and C, in certain cases) denote the levels 5, 10, 30, 50, and 100 mm, respectively, above the chill end (*i.e.*, cooling rates corresponding to DASs of 16, 23, 47, 61, and 83 μm for the 319 alloys and 15, 23, 39, 53, and 75 μm for the A356.2 alloys).

1. Platelet size of β -Al₅FeSi

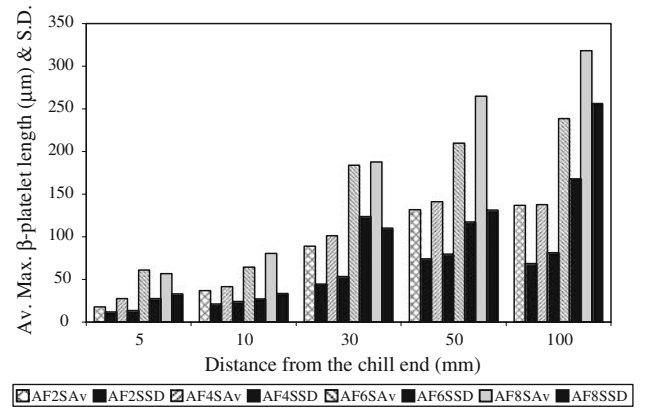
The data shown in Tables II through IV were plotted in the form of histograms for both nonmodified and Sr-modified alloys. Figures 9 through 11 depict these histograms, showing the average maximum β -platelet lengths obtained as a function of distance from the chill end (*i.e.*, cooling rate) for the three types of alloy. The results may be summarized as follows.

2. Alloy A319.2

With regard to the cooling rate, it can be observed that the higher the cooling rate (*i.e.*, at distances of 5 and 10 mm from the chill end), the shorter the β -platelet average maximum length in both nonmodified and Sr-modified alloys (*e.g.*, 31.02 μm for the AF4-0 alloy vs 143.14 μm for the AF4-C alloy, and 27.58 μm for the AF4S-0 alloy vs 137.71 μm for the AF4S-C alloy). There are two possible explanations, as follows: (1) a higher cooling rate will increase the maximum solubility of Fe in the aluminum matrix, resulting in finer β particles, and (2) a higher cooling rate will also result in a smaller



(a)



(b)

Fig. 9—Effect of cooling rate on the average maximum β -platelet length observed in (a) nonmodified and (b) Sr-modified A319.2 alloys.

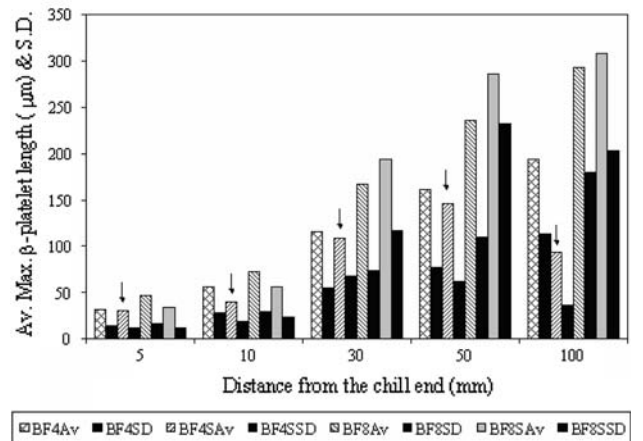
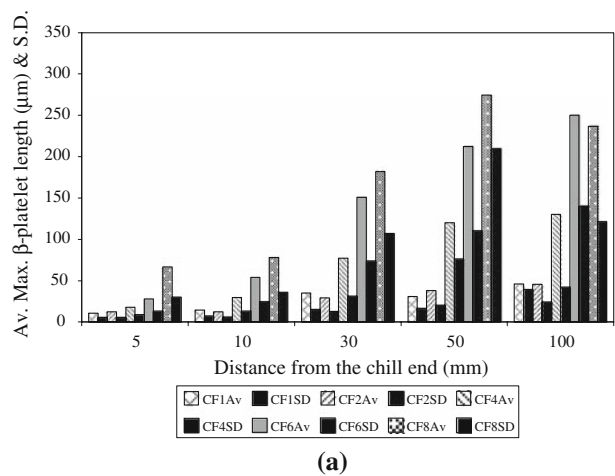


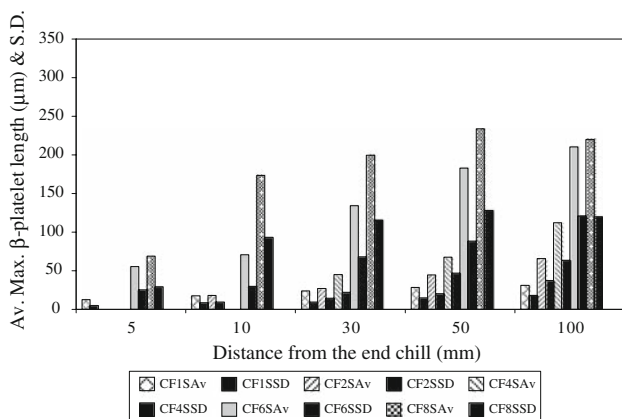
Fig. 10—Effect of cooling rate on the average maximum β -platelet length observed in nonmodified and Sr-modified B319.2 alloys. Arrows refer to Sr-modified alloys.

DAS, and the overall refinement of the microstructure will result in the precipitation of finer β particles.

At higher cooling rates, the effect of the Sr addition on the β -platelet length is not immediately obvious, while the effect resulting from the cooling rate is



(a)



(b)

Fig. 11—Effect of cooling rate on the average maximum β -platelet length observed in (a) nonmodified and (b) Sr-modified A356.2 alloys.

stronger than that from the Sr modification. At lower cooling rates, the β -platelet lengths in the higher Fe-level alloys are longer in the Sr-modified alloys than they are in the nonmodified alloys. In this case, the addition of Sr poisons the β -needle nucleation sites. Consequently, the β -Fe phase must precipitate at a smaller number of sites, resulting in the precipitation of needles that are larger than those in the nonmodified alloys. This scientific observation is in contrast to the observations recorded by Shabestari and Gruzleski,^[14,15] who reported that for slow cooling rates, Sr causes fragmentation of the β needles and a 47 pct reduction in volume, which is ultimately transformed into sludge.

It can also be observed that the higher the iron content, the longer the β -platelet lengths, especially at the lowest cooling rate (117.72 μm for the AF2-C alloy, with 204.75 μm for the AF8-C alloy). This datum is in accordance with the work of Pennors *et al.*,^[24] who observed that an increased Fe content results in the precipitation of the long, thick needles/platelets typical of the β -Al₅FeSi intermetallic phase.

3. Alloy B319.2

In this case also, the higher the cooling rate, the shorter the average maximum β -platelet length

observed. As regards the 0.4 pct Fe-containing alloy, the addition of 250 ppm Sr does, in fact, decrease the β -platelet length at a number of different cooling rates (arrows in Figure 10).

The addition of 250 ppm Sr at 0.8 pct Fe levels decreases the β -platelet length at higher cooling rates, at DAS values up to $\sim 16 \mu\text{m}$, but increases the length at lower cooling rates, at DAS levels of $\sim 76 \mu\text{m}$ or more. It will also be observed that the higher the iron content, the longer the β -platelet length, especially at the lowest cooling rate.

4. Alloy A356.2

In this case, also, as Figure 11(a) shows, the β -platelet lengths increase with a decrease in the cooling rate in the unmodified alloys. The Sr-modified alloys also show the same trend with respect to the cooling rate. In comparison with the unmodified alloys, however, the β -platelet lengths at cooling rates corresponding to levels of up to 30 mm in distance from the chill end are longer in the modified alloys, particularly at Fe levels of 0.6 and 0.8 pct, but are shorter at cooling rates corresponding to levels of 50 and 100 mm above the chill end, as may be observed in Figure 11(b). It may also be seen that the β -platelet lengths increase with the increase in Fe content, as was expected to be the case. The observations made in regard to the Sr-modified alloys result from a combined effect of the Fe, the cooling rate, and the effect of Sr on the fragmentation and dissolution of the β -Al₅FeSi phase.

5. Platelet density of β -Al₅FeSi

Figures 12(a) through (c) show plotted charts of the β -platelet density vs cooling rate for the three alloys under the unmodified and Sr-modified conditions. While the plots for all three alloy types appear to be essentially similar, the following features justify being highlighted.

- The difference between the β -platelet densities in the various alloys is more evident at the higher cooling rates and, after a DAS of $\sim 43 \pm 4 \mu\text{m}$ corresponding to the 30-mm level above the chill end, the density remains more or less the same, irrespective of the Fe content of the alloy or whether it is modified.
- For the various Fe levels, the modified alloys exhibit the highest β densities at the highest Fe levels (0.8 pct Fe in the A319.2 and B319.2 alloys, and 0.6 pct Fe in the A356.2 alloy). At lower Fe levels, no clear distinction can be drawn.
- In the B319.2 alloy (containing 0.4 pct Mg), except for the jump in density observed at the lowest cooling rate for the B4S alloy, both modified and unmodified alloys display identical, or at least very similar, β -platelet densities.

The presence of a sufficiently high concentration of Sr leads to a breakdown of the β platelets into smaller, thinner fragments *via* the following two mechanisms:^[25] (1) the splitting of the needle/platelets into two halves through the formation of longitudinal cracks, which is enhanced greatly by the brittle nature of the β -iron phase, and (2) fragmentation due to Si rejection on

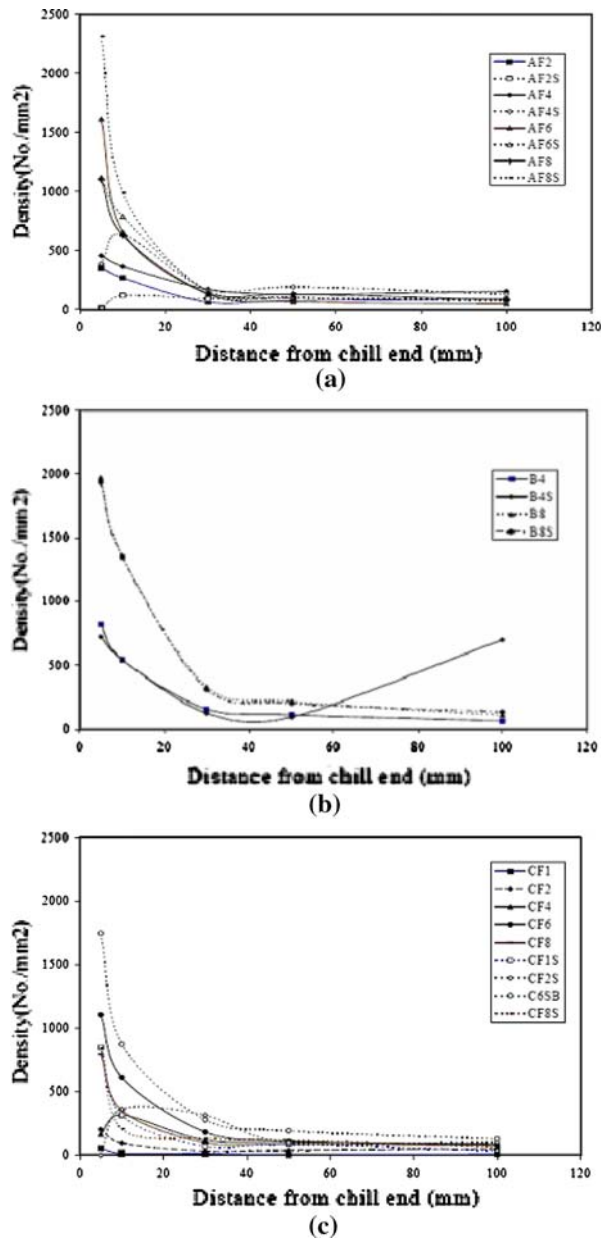


Fig. 12—Effect of cooling rate on the β -platelet density observed in (a) A319.2 alloys, (b) B319.2 alloys, and (c) A356.2 alloys.

account of this; there is an effective increase in the density, with the addition of Sr, compared to the unmodified case. At low cooling rates, the iron intermetallics grow to large sizes, and thus particle density is reduced to a minimum.

It was observed by Villeneuve and Samuel^[25] that the Sr addition only affects small β needles; this phenomenon is more pronounced in high-Fe-containing alloys. On the other hand, large β needles are seen to persist, even after a Sr addition or solution heat treatment. This would explain the collective features of the β -iron intermetallic density plots in Figures 12(a) through (c). In the case of the B319.2 alloys, Mg-Sr interactions as a result of the presence of Mg reduce the effect of the Sr.

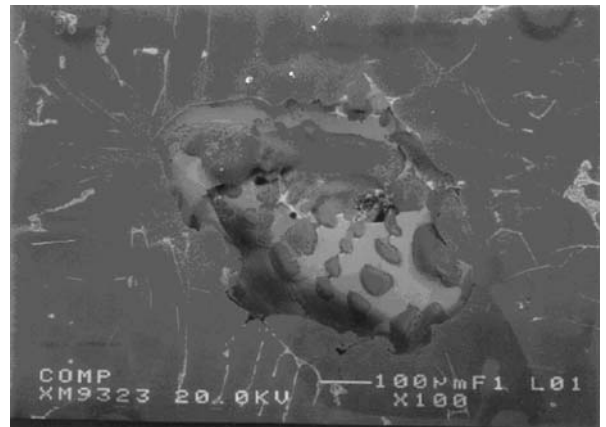


Fig. 13—SEM micrograph taken from the Sr-modified A319.2-0.4 pct Fe alloy, showing the dissolution effect of Sr on the β -Al₅FeSi phase.

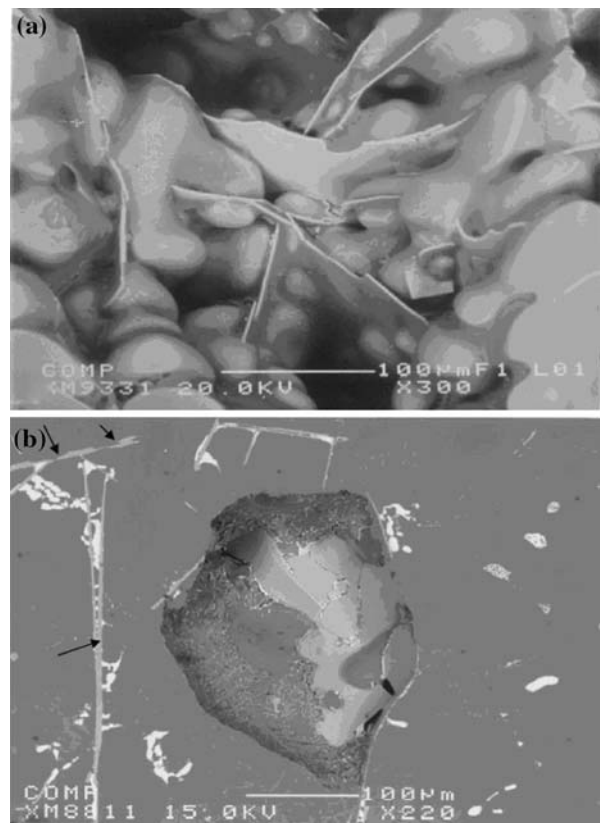


Fig. 14—Backscattered images of (a) nonmodified and (b) Sr-modified A319.2-0.8 pct Fe alloy showing β -Al₅FeSi platelet characteristics.

Thus, both unmodified and Sr-modified alloys display very similar densities at all cooling rates. Also, as will be discussed in Section C, due to the presence of 0.026 pct Mn in the alloy, several α -iron intermetallics were also observed in the microstructure of the B8 alloy, thus providing a further reason for the similarity to be observed in the densities of the β -iron intermetallic.

C. Mechanism of β -Al₅FeSi Fragmentation

The backscattered images shown in Figures 13 and 14 reveal the influence of Sr in the fragmentation and dissolution of the β -Al₅FeSi phase. It is in this context that “Sr modification” is understood with respect to the β -iron phase. As a result of the dissolution effect of Sr, the α -Al dendrites appear through regions of the β -Al₅FeSi platelet in which dissolution has taken place, as may be seen in Figure 13, while the β -platelet may be observed within a shrinkage pore in the A319.2 alloy containing 0.4 pct Fe. Other β -Al₅FeSi platelets (or needles, as they appear in the micrograph) are fine in appearance, whether of small or medium size.

As compared to the preceding sample, the β -Al₅FeSi needles observed in the backscattered image taken of the A319.2 alloy sample containing 0.8 pct Fe, Figure 14(a) shows the profusion of β platelets that occur at such high Fe levels. The three-dimensional nature of the linking of these platelets may clearly be observed within the pore shown in this image; such β platelets appear as branched β platelets in a two-dimensional optical micrograph.

It is worth noting that the β platelets appear to be solid in nature, thereby indicating that Sr has no effect upon these platelets. Also, the fact that the α -Al dendrites appear in their natural rounded form indicates that the pore under observation is a shrinkage pore and that the porosity results from the blocking effect of the β platelets on the liquid metal flow during the solidification process. Thus, the porosity observed in conjunction with the β -iron platelets results from feedability-associated problems.

The backscattered image taken of the Sr-modified sample (same alloy) shown in Figure 14(b) depicts an example of a β -Al₅FeSi platelet within a rounded pore, in which the progress of fragmentation of the β platelet is evident. Modified eutectic Si regions and α -Al dendrites (flat, dark gray areas) may also be observed around the β platelet. The flattened nature of the dendrites as well as the rounded morphology of the pore indicates that this is a gas pore. Elsewhere in the matrix, other β platelets (light gray needles) and CuAl₂ intermetallic particles (white) may also be seen. The dissolution effect of Sr on the β platelet in the upper left corner of the figure may clearly be seen (arrowed), while the much larger β platelet perpendicular to it appears to be unaffected. The two backscattered micrographs in Figure 14 demonstrate that the smaller-sized coeutectic and posteutectic β platelets are easily fragmented as a result of the action of Sr, whereas large, pre-eutectic platelets resist modification and are not easily affected by the presence of strontium.

IV. CONCLUSIONS

An extensive study was carried out to investigate the metallurgical parameters controlling the microstructural evolution of Al-Si-Cu and Al-Si-Mg alloys, in which the microstructural characteristics of directionally solidified 319- and A356-type alloys were examined as a function

of iron content, Sr addition, and cooling rate. By analyzing the effects of these parameters on the precipitation of β -Al₅FeSi iron intermetallic phase, the following main conclusions may be drawn.

1. For the range of cooling rates covered in the present study (corresponding to DASs of ~15 to 85 μ m), the highest cooling rate (at a 5-mm distance from the chill) is the more significant parameter in controlling the size and distribution of the β -Al₅FeSi intermetallic phase in the nonmodified 319 and 356 alloys.
2. At the highest levels of iron (~0.8 pct Fe) and lowest level of cooling rate (at a 100-mm distance from the chill), sympathetic nucleation of the β -Al₅FeSi is observed in the nonmodified alloys, which produces large β -needle entities that extend up to as much as ~200, 300, and 230 μ m across the matrix surface of the A319.2, B319.2, and A356.2 alloys, respectively.
3. The addition of strontium enormously reduces the sympathetic nucleation, through its poisoning action on the β -Al₅FeSi nucleation sites, and a lower β -needle density is obtained (albeit somewhat larger-sized needles) compared to that in the nonmodified alloys. Dissolution of β needles is also observed with the Sr addition, resulting in the fragmentation of coeutectic or posteutectic β -Al₅FeSi platelets.
4. The effect of strontium on the fragmentation of β -Al₅FeSi phase (*i.e.*, in decreasing its size) at high DASs in the A319.2 alloy is effective at lower iron levels, *viz.* below 0.6 wt pct Fe. For the B319.2 and A356.2 alloy, the effect is more evident at low DASs.
5. For the various Fe levels, the Sr-modified alloys exhibit highest β densities at the highest Fe levels (0.6 pct Fe in the A319.2 and B319.2 alloys, and 0.8 pct Fe in the A356.2 alloy). At lower Fe levels, no clear distinction can be drawn.

ACKNOWLEDGMENTS

Grateful acknowledgment is hereby extended to the Natural Sciences and Engineering Research Council of Canada (NSERC), the General Motors Powertrain Group (Milford, NH), Corporativo Nemak (Garza Garcia, NL, Mexico), the Fondation de l'Université du Québec à Chicoutimi (FUQAC) (Chicoutimi, QC, Canada), and the Centre québécois de recherche et développement de l'aluminium (CQRDA) (Chicoutimi, QC, Canada) for financial assistance received in the form of scholarships and in-kind support.

REFERENCES

1. P.N. Crepeau: *AFS Trans.*, 1995, vol. 103, pp. 361–66.
2. S. Nishi, T. Shinoda, and E. Kato: *J. Jpn. Inst. Light Met.*, 1968, vol. 18 (12), pp. 627–35.
3. D.L. Colwell and R.J. Kissling: *AFS Trans.*, 1961, vol. 69, pp. 610–15.

4. R.C. Lemon and H.Y. Hunsiker: *AFS Trans.*, 1956, vol. 64, pp. 255–60.
5. M. Tsukuda, M. Harada, T. Suzuki, and S. Koike: *J. Jpn. Inst. Light Met.*, 1978, vol. 28 (3), pp. 109–15.
6. F.A. Badia: *Mod. Cast.*, 1966, vol. 49, pp. 104–15.
7. J.E. Hatch: *Aluminum: Properties and Physical Metallurgy*, ASM, Metals Park, OH, 1984, pp. 320–50.
8. D.O. Northwood, X.C. Sun, G.E. Byczynski, and J.H. Sokolowski: *Proc. Int. Symp. on Recent Metallurgical Advances in Light Metals Industries, 34th Annual Conf. of Metallurgists of CIM*, S. MacEwen and J.P. Gilardeau, eds., Vancouver, BC, 1995, pp. 355–65.
9. L.A. Narayanan, F.H. Samuel, and J.E. Gruzleski: *Metall. Mater. Trans. A*, 1994, vol. 25A, pp. 1761–73.
10. D.A. Granger: *AFS Trans.*, 1991, vol. 99, pp. 379–83.
11. L. Bäckerud, G. Chai, and J. Tamminen: *Solidification Characteristics of Aluminum Alloys*, vol. 2, *Foundry Alloys*, AFS/Skanaluminium, Des Plaines, IL, 1990, pp. 71–84.
12. G. Gustafsson, T. Thorvaldsson, and G.L. Dunlop: *Metall. Trans. A*, 1986, vol. 17A, pp. 45–52.
13. D.A. Granger, R.R. Sawtell, and M.M. Kersker: *AFS Trans.*, 1984, vol. 92, pp. 579–86.
14. S.G. Shabestari and J.E. Gruzleski: *Cast Met.*, 1994, vol. 6 (4), pp. 217–24.
15. S.G. Shabestari and J.E. Gruzleski: *Cast Met.*, 1994, vol. 6 (4), pp. 241–51.
16. A.M. Samuel, H.W. Doty, and F.H. Samuel: *Proc. 4th Int. Conf. on Molten Aluminum Processing*, Orlando, FL, AFS, Des Plaines, IL, 1995, pp. 261–94.
17. A.M. Samuel, F.H. Samuel, and H.W. Doty: *J. Mater. Sci.*, 1996, vol. 31, pp. 5529–39.
18. L.A. Narayanan, F.H. Samuel, and J.E. Gruzleski: *Metall. Mater. Trans. A*, 1995, vol. 26A, pp. 2161–74.
19. M. Drouzy and M. Richard: *Fonderie*, 1969, vol. 285, pp. 500–04.
20. J.C. Jaquet and H.J. Huber: *Geissereiforschung*, 1985, vol. 38 (1), pp. 11–20.
21. K.J. Oswalt and M.S. Misra: *AFS Trans.*, 1980, vol. 88, pp. 845–62.
22. H. Samuel, P. Ouellet, A.M. Samuel, and H.W. Doty: *Metall. Mater. Trans. A*, 1998, vol. 29A, pp. 2871–84.
23. C. Mascré: *Fonderie*, 1955, vol. 108, pp. 4330–36.
24. A. Pennors, A.M. Samuel, and F.H. Samuel: *ASF Trans.*, 1998, vol. 106, pp. 251–70.
25. C. Villeneuve and F.H. Samuel: *Int. J. Cast Met. Res.*, 1997, vol. 12, pp. 145–60.